Propulsion Force Analysis of Superconducting Coils in a Planar Actuator Application

Weultjes, Ryan

Award date:
2023

Msc. Thesis

Automotive Technology, Electromechanics specialisation track

Propulsion Force Analysis of Superconducting Coils in a Planar Actuator Application

(Temporary publicly available version due to confidentiality)

RYAN WEULTJES, R.W.

Thesis supervisors:	dr. ir. B. van Ninhuijs
	dr. ir. D.C.J. Krop
Comittee members:	dr. ir. D.C.J. Krop
	prof.dr. E.A. Lomonova
	dr.ir. I.J.M. Besselink
Advisory comittee members:	ir. A. Desikan
	dr. ir. B. van Ninhuijs
Student number:	1484052
Graduation year:	2023
European credits:	45
Confidentiality period:	2 years
Publication date:	December 2024

This report was made in accordance with the TU/e Code of Scientific Conduct for the Master thesis.

Propulsion Force Analysis of Superconducting Coils in a Planar Actuator Application

R. Weultjes
VDL ETG, Eindhoven, The Netherlands

***Abstract*—This paper concerns an analysis of the relative propulsion force performance that could be obtained by the implementation of superconducting coils instead of permanent magnets in a planar actuator (PA) application. The PA configuration in consideration consists of moving copper coils and stationary High-Temperature-Superconducting (HTS) coils producing a constant magnetic field. The HTS coil array is modelled by the Biot-Savart law, which is modelled by a series of current sheets for a squircle and a circular coil geometry. These current sheets are obtained by numerical integration of infinitesimally thin line sources. The operating limits are mandated by the maximum allowable mechanical stress of the HTS coils which is obtained from the Lorentz force equation. And the maximum current handling capability of the superconductor is obtained from a measurement set for various tape variants and operating temperatures. The expected model error of B_z is equal to 60μT in relation to a maximum amplitude of 166mT. And the quench current is predicted 12$\%$ up to 20$\%$ higher than the actual quench current of the coil. A relative propulsion force evaluation metric is introduced to evaluate the magnetic field of an HTS coil PA-variant by comparing it to a permanent magnet variant.**

***Index Terms*—planar actuator, analytical model, Biot-Savart, superconducting, HTS operating limits, propulsion force**

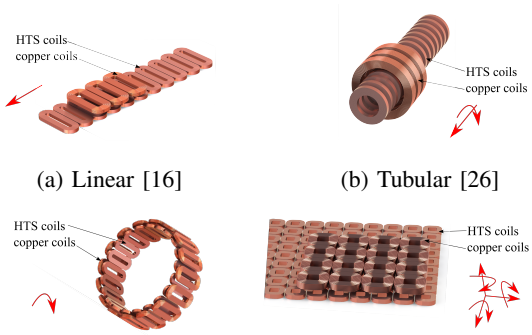

(a) Linear [16] (b) Tubular [26]

(c) Rotating [33] (d) Planar

Figure 1: Overview of 4 different HTS actuator types published in literature.

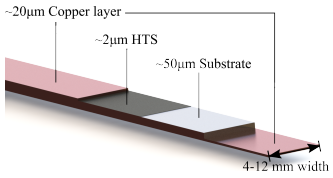

Figure 2: Overview of the composition and typical dimensions offered by HTS tape manufacturers.

I. Introduction

ACHIEVING a high force or power density in electric machine design is important for many applications such as transportation [1]–[5], renewable energy [6]–[8] and automation solutions [9]–[11]. A promising technology to increase the force density of actuators is the use of superconducting coils since it allows for a higher magnetic field strength in electric machines compared to copper coils or permanent magnets [12]–[16]. Several machine designs based on High-Temperature Superconducting (HTS) coils manufactured from superconducting tape have been published in the literature. These HTS machines can be classified into the following actuator types: linear [17]–[25], tubular [26]–[28], rotating [29]–[34], and planar [35]–[37], where each actuator type is depicted in Fig. 1.

The use of superconducting tape allows for a significantly higher current density compared to copper wire, due to the relatively low electrical resistivity when the superconductor is in the superconductive state. The superconductor transitions from the superconductive state to a normal conductive state when the current exceeds the critical current, this state transition is referred to as quench. Upon quench, Joules losses are produced due to the increase of electrical resistivity of the HTS material. If the losses exceed the cooling power capability of the system the temperature of the coils increases, thereby increasing the electrical resistivity of the HTS material. This causes thermal runaway of the system, which could cause significant damage to the HTS coil. Typically the critical current through the HTS tape is determined by measurements for specific operating conditions [38], [39]. The critical current for a given tape width is dependent on various environmental factors such as the temperature, magnetic field strength, angle of the magnetic field with respect to the tape and the specific tape variant.

This HTS tape consists of several layers, where the superconductive material is deposited on an alloy substrate for mechanical strength and stiffness as depicted by Fig. 2, which is encapsulated by a layer of copper for thermal conductivity. Most HTS tape manufacturers are using Yttrium Barium Copper Oxide (YBCO) as the superconductive material since

this material yields a high critical current even in applications with a magnetic field strength over 10T [40], [41].

At the moment HTS tape is economically relatively expensive at a cost of approximately €40/m, in combination with low available quantities in relation to copper wire. Hence making it a viable consideration in demanding applications and low-quantity production such as in the high-tech industry. The economic cost and available quantity are expected to improve over time [42] broadening the scope of HTS actuators to other applications in the future.

A relatively fast model is required to verify multiple coil topologies and determine the propulsion force performance that could be achieved. Hence resulting in the research that is shown in this paper.

Several research papers have published various PA designs [43]–[50], and several (currently expired) patents have been filed [51]–[53]. The optimisation of these planar actuators is elaborate [54]–[56], especially when the superconducting properties have to be included. Design optimisations of HTS linear machines are shown by de Bruyn [16] and Desikan [15]. An HTS PA design is proposed by Koolmees [36], although the magnetic design is not optimised and the propulsion force performance that could be achieved is not elaborately explained. An HTS PA design is designed and compared by [37], although a detailed analysis of the maximum current through the superconducting coils is lacking.

This paper presents a method to model a static magnetic field generated by a stationary HTS coil array. And the mechanical stress and quench limits of the HTS coils are taken into consideration to determine the relative propulsion force performance that could be achieved by an HTS PA in relation to a Permanent Magnet (PM) Halbach PA.

First, the magnetic modelling is explained in section II based on the Biot-Savart method. Next, section III describes the operating limits in terms of quench current and mechanical stress limit. Section IV introduces a metric for the relative propulsion force performance of the mover in relation to a PM Halbach PA design. Followed by an evaluation of the modelling evaluation in section V to indicate the expected modelling accuracy for both the magnetic field and the maximum current of the coils.

II. Magnetic Modelling of an HTS Coil Array

This section shows how the magnetic field of an HTS circular or squircle coil array is obtained by the Biot-Savart law in combination with numerical integration to obtain a current sheet from an arc and a line segment. First, the method to obtain the magnetic vector potential from the line segments is explained, followed by the method to obtain the magnetic flux density for the coil array

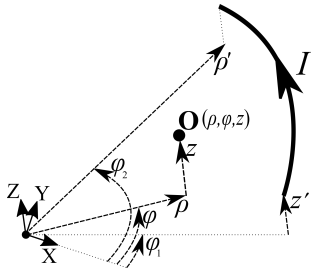

Figure 3: Description of coordinate system parameters used for the filamentary arc segment.

A. The Magnetic Vector Potential of an arc Segment

The method explained in [57] is used to obtain the magnetic vector potential in free space of an infinitesimally thin current line source, in the shape of an arc. Fig. 3 shows the filamentary arc segment in free space with the required coordinates to obtain the magnetic vector potential at a given point in space. The location of the observation point **O** in free space is given by the cylindrical coordinate system (ρ, ϕ, z). The Cartesian coordinates (x, y, z) can be transformed into the cylindrical coordinate system by

$$\rho = \sqrt{x^2 + y^2}, \tag{1}$$

$$\phi = \arctan\left(\frac{y}{x}\right). \tag{2}$$

Additionally, the location of the filamentary arc segment is given by the cylindrical coordinates $(\rho', [\phi_1, \phi_2], z')$, where ϕ_1 and ϕ_2 are the start and end angle of the arc segment respectively. Now the magnetic vector potential parallel to the x and y plane, respectively given by $A_{x,arc}$ and $A_{y,arc}$ is equal to

$$A_{x,arc} = -\frac{\mu_0 I}{4\pi\rho}\Big[\cos(\phi) f_1(\phi') + \sin(\phi) f_2(\phi')\Big]_{\phi'=\phi_1}^{\phi_2}, \tag{3}$$

$$A_{y,arc} = -\frac{\mu_0 I}{4\pi\rho}\Big[\sin(\phi) f_1(\phi') - \cos(\phi) f_2(\phi')\Big]_{\phi'=\phi_1}^{\phi_2}. \tag{4}$$

Where μ_0 is the permeability of vacuum, I is the current through the infinitesimally thin line source, ϕ' is the parameter for the integration boundary limits. The functions $f_1(\phi')$ and $f_2(\phi')$ are respectively given by

$$f_1(\phi') = \sqrt{\rho'^2 + \rho^2 + (z - z')^2 - 2\rho'\rho\cos(\phi' - \phi)}, \tag{5}$$

$$f_2(\phi') = \frac{\rho'^2 + \rho^2 + (z - z')^2}{\sqrt{(\rho' + \rho)^2 + (z - z')^2}}\,\mathbf{F}(\theta, m) - \sqrt{(\rho' + \rho)^2 + (z - z')^2}\,\mathbf{E}(\theta, m). \tag{6}$$

where $\mathbf{F}(\theta, m)$ and $\mathbf{E}(\theta, m)$ are the incomplete elliptical integrals of the first and second kind respectively. θ and m are parameters for the incomplete elliptical integrals which are given by

$$\theta = \frac{\phi' - \phi - \pi}{2}, \tag{7}$$

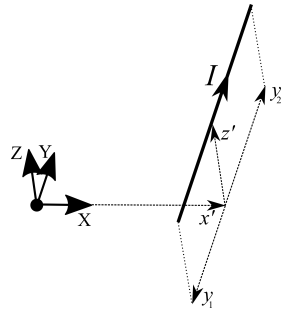

Figure 4: Description of coordinate system parameters used for the filamentary line segment.

$$m = \frac{4\rho'\rho}{(\rho' + \rho)^2 + (z - z')^2}. \tag{8}$$

A method for fast computation of the incomplete elliptical integrals is shown in appendix A.

B. The Magnetic Vector Potential of a Line Segment

The magnetic vector potential of an infinitesimally thin line segment is obtained with the Biot-Savart law. Where the magnetic vector potential of a line segment $A_{x,line}$ parallel to the x plane is given by

$$A_{x,line} = \frac{\mu_0 I}{4\pi} \int_{y_1}^{y_2} \frac{1}{\sqrt{(x - x')^2 + (y - y')^2 + (z - z')^2}}\, dy', \tag{9}$$

where (x, y, z) are the cartesian coordinates of the observation point in free space, and (x', y', z') are the cartesian coordinates of the line segment, and y_1, y_2 are the start and end location of the line segment respectively. All of the coordinates used to describe the line position are shown in Fig. 4. By solving (9) the following result is obtained for $A_{x,line}$ which is equal to

$$A_{x,line} = -\frac{\mu_0 I}{4\pi}\Big[\log\Big(-y + y' \cdot \sqrt{x^2 - 2x \cdot x' + x'^2 + y^2 - 2y \cdot y' + y'^2 + z^2 - 2z \cdot z' + z'^2}\Big)\Big]_{y'=y_1}^{y_2} \tag{10}$$

where y' is the parameter for the integration boundary limits.

C. Obtaining the B-field of an HTS Coil Array

The magnetic flux density for a line source B_{line} is obtained by taking the curl of the magnetic vector potential of a line source A_{line}.

$$B_{line}(I) = \nabla \times A_{line}(I) \tag{11}$$

The magnetic field of a squircle coil is created by the combination of an arc segment and a line segment, as shown in Fig. 5. And the magnetic field of a circular coil just consists of the arc segment. By rotating and adding the result of a quarter loop a full loop can be obtained. Now a current sheet can be obtained by numerical integration from a series of equally spaced

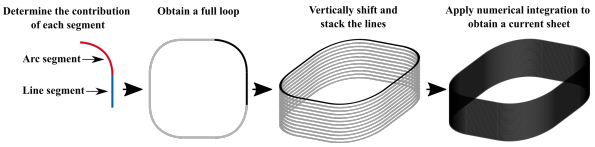

Figure 5: Explanatory drawing of how to obtain a current sheet from an arc and line segment.

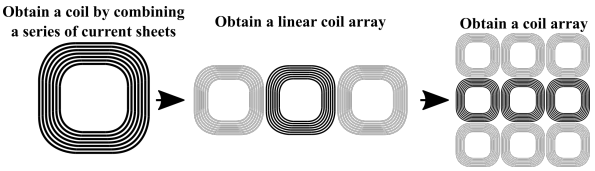

Figure 6: Expalantory drawing how to obtain a coil array from a series of current sheets.

stacked line sources. The magnetic flux density of a current sheet B_{sheet} can be obtained by

$$B_{sheet}(\kappa) = \int_0^{w_t} \vec{B}_{line}(\kappa)\, \mathrm{d}z. \tag{12}$$

Where w_t is the width of the tape, and κ is the sheet current density which is equal to

$$\kappa = \frac{I}{w_t}, \tag{13}$$

where w_t is the width of the tape. An HTS coil can be modelled by combining a series of these current sheets with superposition located at the position of the HTS material in the coil. The superposition principle can be applied as long as the application only consists of linear relationships, which holds since no back-iron is expected to be used in the implementation and the highly non-linear electric properties of the HTS tape are not simulated. Fig. 6 shows how a coil array can be obtained with an alternating pole pattern by using the superposition principle. First, the magnetic field of a single coil is translated horizontally and the phase of the magnetic field is inverted to ensure the alternating pole polarity. Next, the sum of the magnetic field is taken from the original and the translated coil to obtain the field of a linear coil array. Subsequently, the magnetic field of a coil array is obtained by implementing the same aforementioned steps, by using the magnetic field of a linear coil array and implementing vertical shifting of the magnetic field.

III. Operating Limits of the HTS Tape

The magnetic performance of the coil array is limited by the current handling capability and maximum tolerable mechanical stress in the tape.

A. Mechanical Stress Limit of HTS Tape

The mechanical stress in the tape is modelled from the Lorentz force equation. Where the force density f is equal to

$$f = \rho \cdot E + J \times B, \tag{14}$$

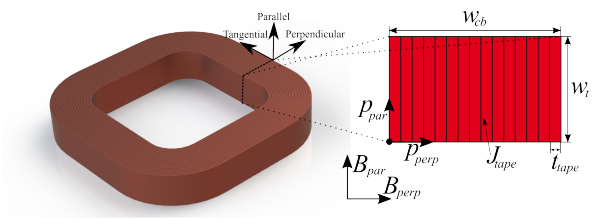

Figure 7: Description of the used coordinate system to obtain the mechanical stress in the coil.

where ρ is the free charge density, E is the electric field, J is the current density, B is the external B-field. The contribution of the free charge density and the E-field is neglected, due to the significantly smaller contribution in relation to the cross product of J and B. It is assumed that the mechanical stress due to Lorentz forces in the parallel direction distributes homogeneously over the tape thickness t_{tape}, due to the high stiffness of the substrate. This assumption is implemented by using a current density, which is homogeneously distributed over the tape J_{tape}. That is equal to

$$J_{tape} = \frac{I}{t_{tape} \cdot w_t}, \tag{15}$$

where t_{tape} is the tape thickness. The mechanical stress experienced by the coil is obtained by the integration of the force density given by (14), leading to the parallel and perpendicular stress σ_{par} and σ_{perp}. Which is equal to

$$\sigma_{par} = -\int_0^{w_t} B_{perp} \cdot J_{tape} \, \mathrm{d}p_{par}, \tag{16}$$

$$\sigma_{perp} = \int_0^{w_{cb}} B_{par} \cdot J_{tape} \, \mathrm{d}p_{perp}. \tag{17}$$

Where p_{par} and p_{perp} is the parallel and perpendicular position in the coil section respectively, B_{par} and B_{par} are the parallel and perpendicular B-field with respect to the direction of the tape, w_{cb} is the coil bundle width. The used parameters and coordinate system are depicted by Fig. 7. The normalised mechanical stress γ is equal to

$$\gamma = \sqrt{\left(\frac{\sigma_{perp}}{\sigma_{perp,max}}\right)^2 + \left(\frac{\sigma_{par}}{\sigma_{par,max}}\right)^2}. \tag{18}$$

Where $\sigma_{perp,max}$, $\sigma_{par,max}$ is the mechanical stress limit of the tape in the perpendicular and parallel direction respectively.

The maximum allowable compressive stress without significant critical current degradation is measured by Fujikura given by [58]. It is assumed that the tape of Fujikura behaves mechanically equal due to the similar composition of tape layers and materials. Additionally, the assumption is made that the maximum allowable mechanical stress scales proportional to the relative substrate thickness. Since the substrate has a significantly higher stiffness and strength in relation to the other materials present in the HTS coil [59]–[61]. The maximum allowable mechanical stress σ_{max} in the parallel and perpendicular direction scales proportionally to the relative substrate thickness. Hence the maximum mechanical stress $\sigma_{max,ref}$ is equal to

Table I: Measured mechanical stress limits of the HTS tape without significant critical current degradation [58].

Dimension	Parameter	Value	Unit
Parallel stress reference	$\sigma_{par,ref}$	100	MPa
Perpendicular stress reference	$\sigma_{perp,ref}$	400	MPa
Substrate reference thickness	$t_{sub,ref}$	50	μm

$$\sigma_{max} = \sigma_{max,ref} \cdot \left(\frac{t_{sub}}{t_{sub,ref}}\right). \tag{19}$$

Where t_{sub} is the substrate thickness of the HTS tape, and $t_{sub,ref}$ is the reference substrate thickness used in the measurement by Fujikura, which is shown in Tab. I.

B. Current Handling Capability of HTS tape

The maximum current handling capability of the HTS tape is limited by the critical sheet current density κ_c. Typically the critical voltage criterion E_0 is used to predict the quench limit of the superconductor, where an E-field threshold of 1μV/cm is often used for high temperature superconductors [62]–[66]. Hence quench is expected when the current sheet density κ exceeds the critical current sheet density κ_c. This relative quench limit is denoted by the normalized critical current sheet density κ_n which is equal to

$$\kappa_n(T, \kappa_c, \kappa, \vec{B}_{tape}) = \frac{\kappa}{\kappa_c(T, \vec{B}_{tape}(\kappa))}. \tag{20}$$

This is dependent on the temperature T, κ_c is the critical sheet current density which is obtained from a database for operating conditions further explained in appendix B, $\vec{B}_{tape}$ is the B-field experienced by the tape in the parallel and perpendicular direction respectively being B_{par} and B_{perp}. It should be noted that κ_c is dependent on the temperature and the magnetic field which in turn is dependent on the current sheet density. Hence this normalized critical sheet current density scales highly non-linear to the operating conditions. The quench current sheet density κ_{quench} is expected when the normalised critical sheet current density equals 1, leading to the following optimisation problem for κ_{quench}.

$$\kappa_{quench} = \min_{\kappa} \quad \kappa_n\Big(V_{tape},\, T,\, \kappa,\, \vec{B}_{tape}(G, \kappa)\Big) \,-\, 1$$
$$\text{s.t.} \quad (\kappa_n - 1) > 0 \tag{21}$$

Many of the parameters are expected to remain constant during a parameter sweep for various actuator

configurations, such as the used HTS tape variant V_{tape}, the temperature T, and the coil geometry G. The B-field scales linear proportional to the current sheet density from the initially simulated magnetic field B_{init} in relation to the initial simulation current sheet density κ_{init}. Which is given by the equation

$$\vec{B}_{tape}(G,\, \kappa_{init},\, \kappa) = \vec{B}_{init}(G,\, \kappa_{init}) \cdot \frac{\kappa}{\kappa_{init}}. \tag{22}$$

The linear scaling of the magnetic field in (22) is applicable since no non-linear properties are simulated in the magnetic field simulation.

The optimisation problem given by (21) is computationally relatively expensive. Hence the quench sheet current density is obtained in advance by solving (21) with linear interpolation with a spline curve over a wide range and storing the result in a lookup table. The quench sheet current density can now be expressed as a function of the tape variant, operating conditions, and the magnetic field $\kappa_{quench}\left(V_{tape},\, T,\, \kappa_{init},\, \vec{B}_{init}\right)$.

IV. Obtaining a Propulsion force Performance Metric of an HTSPA

The relative acceleration performance of the HTS planar actuator is obtained by comparing the relative performance that could be achieved by a permanent magnet planar actuator. The first harmonic of the magnetic field is evaluated in the mover coils to compare both actuator types.

A. Obtaining the Magnetic Performance of the HTS Coil Plate

The propulsion force of a moving coil PA is only dependent on the magnetic field present in the vertical plane B_z [67], and the interaction of the mover coils. Where the mover coil design has been kept the same in this research, hence neglecting the contribution of the mover coils. The 1st harmonic of B_z produces most of the propulsion force, and the higher components mainly introduce force and torque disturbance in the mover [68]. A 2-dimensional discrete Fourier transform is used to obtain the 1st harmonic out of B_z in the mover coils [69]. The Fourier transform requires a periodic signal up to the maximum acceptable harmonic given by the *Nyquist-rate* [70]. The magnetic field is obtained only from the centre coil out of a 3x3 coil array. To negate most of the end-effects present in the coil array without obtaining a significant penalty to computational speed. The periodicity of the magnetic field is obtained by converting the single pole field to a 2x2 alternating north-south pole pattern, by using superposition. The harmonic information of B_z for each harmonic k is denoted by $B_{z,k}$, which can be obtained from the periodic magnetic field which

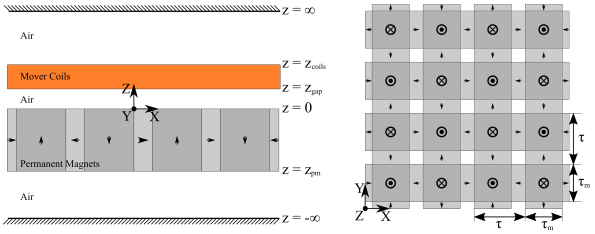

Figure 8: Overview of the Halbach magnet grid and the correlating parameters used in the harmonic modelling.

requires an equal pole pitch in the x and y direction. Now $B_{z,per}$ can be obtained by

$$B_{z,k}(k) = \frac{4}{N_x \cdot N_y} \sum_{n_x=1}^{N_x} \sum_{n_y=1}^{N_y} B_{z,per}(n_x,\, n_y) \cdot \mathrm{e}^{-i2\pi \cdot k \cdot (\frac{n_x}{N_x} + \frac{n_y}{N_y})}. \tag{23}$$

The index in the x and y direction are respectively denoted by n_x and n_y and the total number of indices in each direction are respectively equal to N_x and N_y, and $B_{z,per}$ is the periodic magnetic field.

B. Magnetic Modelling of a PM PA

A model of a magnet plate of permanent magnets is required to set a benchmark of the propulsion force performance that could be achieved by a PM PA. A periodic model is used to model the magnetic field of a permanent magnet plate, based on the work published by Jansen [71]. No back-iron is modelled, since the use of back-iron has little effect in a Halbach configuration [72], [73]. The vertical magnetic flux density from the permanent magnets $B_{z,pm}$ is equal to

$$B_{z,pm}(k) = -\frac{B_{rem}}{2} \sum_{k=1}^{\infty} b_k (b_k + a_k\sqrt{2}) e^{-z\lambda} (\mathrm{e}^{z_{pm}\lambda} - 1) \sin(c_2 x) \sin(c_2 y), \tag{24}$$

where B_{rem} is the remanent magnetization of the permanent magnet, x, y and z are the Cartesian coordinates of the observation location, z_{pm} is the lower bound of the permanent magnet plate, and λ is equal to

$$\lambda = c_2\sqrt{2}, \tag{25}$$

and c_2 is equal to

$$c_2 = \frac{k\pi}{\tau}. \tag{26}$$

Additionally a_k and b_k are respectively equal to

$$a_k = \frac{4}{k\pi} \cos\left(\frac{\tau_m c_2}{2}\right) \sin\left(\frac{k\pi}{2}\right), \tag{27}$$

$$b_k = \frac{4}{k\pi} \sin\left(\frac{\tau_m c_2}{2}\right) \sin\left(\frac{k\pi}{2}\right), \tag{28}$$

where τ is the pole pitch, and τ_m is the width of the vertically oriented Halbach magnet. An overview of the used parameters and modelling assumptions is shown in Fig. 8

C. Obtaining the Relative Propulsion Force Performance of the HTS PA

The HTS and PM PA require a different operating height for the mover coils. The PM type requires an air gap of 3mm, and the HTS type requires an additional 7mm for the cryogenic insulation up to a total air gap of 10mm [35]. This difference in air gap height is compensated by integrating the first harmonic in the mover coil height, to obtain a metric for the propulsion force performance of each actuator type. The propulsion force performance metric for the permanent magnets ψ_{pm} is obtained by integrating (24) for the first harmonic k in the mover coils ranging from z_{gap} up to z_{coil}, which is equal to

$$\begin{aligned}\psi_{pm} &= \int_{z_{gap}}^{z_{coil}} B_{z,pm}(k)\,\mathrm{d}z \\ &= -\frac{b_k(\sqrt{2}a_k + b_k)B_{rem}}{2\lambda} \cdot (\mathrm{e}^{z_{pm}\lambda} - 1) \\ &\quad \cdot (\mathrm{e}^{-z_{gap}\lambda} - \mathrm{e}^{-z_{coil}\lambda}) \cdot \sin(c_2 x)\sin(c_2 y).\end{aligned} \tag{29}$$

The propulsion force performance of the HTS PA type ψ_{HTS} is obtained by numerical integration of (23) for the first harmonic in the mover coil height which gives

$$\psi_{HTS} = \int_{z_{gap}}^{z_{coil}} B_{z,k}(k)\,\mathrm{d}z. \tag{30}$$

The relative propulsion force performance of the HTS PA type χ is obtained by comparing the propulsion force performance of the HTS design to the permanent-magnet design. This leads to the following expression for the relative HTS PA propulsion force performance χ which is equal to

$$\chi = \frac{\psi_{HTS}}{\psi_{pm}} \tag{31}$$

The permanent magnet propulsion force performance ψ_{pm} is obtained by performing a parameter sweep over a wide range and obtaining the best performing parameter combination, which is shown in appendix G.

V. Model Verification

The magnetic field modelling accuracy of the Biot-Savart-based model is verified by comparing the result to a FEM simulation performed in Altair Flux. A single squircle coil is simulated, where the magnetic field is observed 10mm above the coil surface. The simulation result and modelling discrepancy of B_z are shown in Fig. 9, and more results and details are shown in appendix H. The simulated discrepancy of the Biot-Savart-based model is equal to 60μT, which is shown by Fig. 9b. If this model discrepancy is evaluated to the maximum simulated B_z-field a modelling discrepancy of 0.04% is obtained.

The assumption of the homogeneous current density distribution in the tape causes a discrepancy of the B_z field in the air gap of roughly 1.1 to 1.8%.

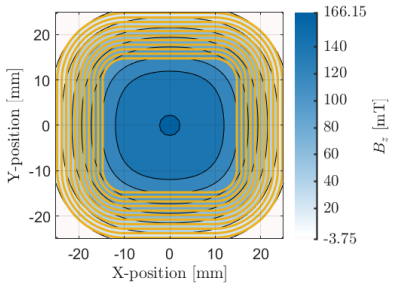

(a) Simulated magnetic field from the Biot-Savart-based model

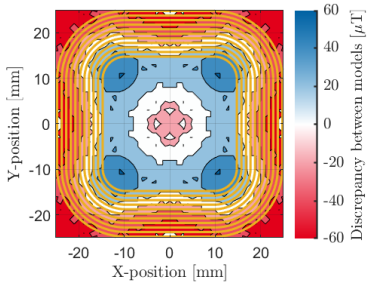

(b) Discrepancy between the Biot-Savart-based model and FEM simulation

Figure 9: Comparison of the magnetic field simulation in the z-direction between the model and a FEM simulation, simulated 10mm above a squircle coil depicted by the yellow lines.

Table II: Overview of the modelled and measured quench current of insulated HTS coils created from Superpower HTS tape validated at 77K.

Publication	Measured I_{quench}	Simulated I_{quench}	Relative discrepancy
[38]	65 A	78 A	+20%
[74] (100μm)	78 A	87 A	+12%
[74] (200μm)	81 A	90 A	+11%

This is determined by a FEM simulation of a single circular insulated HTS coil where the non-linear electrical properties of the HTS material are taken into consideration, which is shown in appendix I.

The quench current modelling accuracy is validated by evaluating the measured quench current I_{quench} to the simulated quench current for equal coil and tape dimensions. Various coils have been validated for the quench current at a temperature of 77K in publications, although none were found at other temperatures for insulated Superpower tape and single pancake coils with an outer diameter of approximately 50mm. The quench current measurements have been obtained from the literature for insulated circular coils manufactured from Superpower HTS tape. In total 3 coil validations have been obtained, which are shown in Tab. II. In the first coil validation, the quench current was simulated 20% above the measured quench current. In the second and third coil validation, the insulation thickness is varied from 100μm up to 200μm with an equal number

of turns. The quench current is simulated at 12% and 11% higher than the measured quench current. It should be noted that the measured quench current is also dependent on the coil fabrication quality and process application [75]. Additionally, careful handling of the HTS tape is crucial not exceeding the minimum bending radius which could lead to a reduced critical current of the HTS tape [76], [77].

VI. Conclusion and Recommendations

The magnetic field generated by the HTS coils is modelled by a Biot-Savart-based model for a squircle coil geometry. The relative propulsion force of the permanent magnet and HTS variant are compared by the integration of the first harmonic of B_z in the mover coil height. The maximum current handling capability of the coil has been limited by the maximum mechanical stress and quench current.

This model could be further elaborated by combining a different current distribution in the HTS tape, with the method proposed by [78]. Although this implementation would increase the computation time of the simulation. A start has now been initiated for an HTS coil topology with relatively well-performing coil dimensions, which allows for faster refinement of the HTS PA design by taking other effects into consideration for example by a FEM model. These other non-simulated effects for example consist of AC losses [16], the current distribution in the coil [15], [78], the mechanical strain of the coil assembly due to the Lorentz force and thermally induced stress [79]–[81], and relative force/torque ripple of the mover [49], [82].

VII. Acknowledgement

I would like to thank dr. ir. D.C.J. Krop and dr. ir. B. van Ninhuijs for the feedback and support during this project. And I would like to thank ir. A. Desikan for the support, discussions about superconducting coils, and the COMSOL simulations. Furthermore, I would like to thank the colleagues from VDL ETG for the helpful discussions and support during this project.

References

[1] R. Hellinger and P. Mnich, "Linear motor-powered transportation: History, present status, and future outlook," *Proceedings of the IEEE*, vol. 97, no. 11, pp. 1892–1900, 2009.

[2] H.-W. Lee, S.-G. Lee, C.-B. Park, J. Lee, and H.-J. Park, "Characteristic analysis of a linear induction motor for a lightweight train according to various secondary schemes," *International Journal of Railway*, vol. 1, no. 1, pp. 6–11, 2008.

[3] S. E. Abdollahi, M. Mirzayee, and M. Mirsalim, "Design and analysis of a double-sided linear induction motor for transportation," *IEEE Transactions on magnetics*, vol. 51, no. 7, pp. 1–7, 2015.

[4] P. J. Masson, T. Nam, T. P. Choi, P. Tixador, M. Waters, D. Hall, C. A. Luongo, and D. N. Mavris, "Superconducting ducted fan design for reduced emissions aeropropulsion," *IEEE Transactions on Applied Superconductivity*, vol. 19, no. 3, pp. 1662–1668, 2009.

[5] Z. Li, R. Zhu, X. Yi, and S. Dong, "A high-power-density piezoelectric actuator operating in bicycling movement mechanism," *IEEE Transactions on Industrial Electronics*, 2022.

[6] P. Jamieson, *Innovation in wind turbine design*. John Wiley & Sons, 2018.

[7] Z. Zhang, A. Chen, A. Matveev, R. Nilssen, and A. Nysveen, "High-power generators for offshore wind turbines," *Energy Procedia*, vol. 35, pp. 52–61, 2013.

[8] Y. Terao, M. Sekino, and H. Ohsaki, "Electromagnetic design of 10 mw class fully superconducting wind turbine generators," *IEEE Transactions on Applied Superconductivity*, vol. 22, no. 3, pp. 5201904–5201904, 2012.

[9] M. P. Kazmierkowski, L. G. Franquelo, J. Rodriguez, M. A. Perez, and J. I. Leon, "High-performance motor drives," *IEEE Industrial Electronics Magazine*, vol. 5, no. 3, pp. 6–26, 2011.

[10] S. E. Lyshevski, V. A. Skormin, and R. D. Colgren, "High-torque density integrated electro-mechanical flight actuators," *IEEE Transactions on Aerospace and Electronic Systems*, vol. 38, no. 1, pp. 174–182, 2002.

[11] Y. Wang, C. Zhi, B. Tang, K. Yang, J. Xie, W. Xu, H. Li, and X. Wang, "A micro electromagnetic actuator with high force density," *Sensors and Actuators A: Physical*, vol. 331, p. 112771, 2021.

[12] R. Qu, Y. Liu, and J. Wang, "Review of superconducting generator topologies for direct-drive wind turbines," *IEEE Transactions on Applied Superconductivity*, vol. 23, no. 3, pp. 5201108–5201108, 2013.

[13] J. Lloberas, "Finite-element analysis of a 15-mw high-temperature superconductor synchronous generator for offshore wind energy applications," *IEEE Transactions on Applied Superconductivity*, vol. 25, no. 6, pp. 1–7, 2015.

[14] R. Qu, Y. Liu, and J. Wang, "Review of superconducting generator topologies for direct-drive wind turbines," *IEEE Transactions on Applied Superconductivity*, vol. 23, no. 3, pp. 5201108–5201108, 2013.

[15] A. Desikan, D. C. Krop, B. d Bruyn, and E. A. Lomonova, "A preliminary study on superconducting linear motors in high-dynamic applications," in *11th International Conference on Power Electronics, Machines and Drives (PEMD 2022)*, vol. 2022, pp. 216–223, IET, 2022.

[16] B. J. H. de Bruyn, *Superconducting linear motors for high-dynamic applications*. PhD thesis, PhD Thesis, Eindhoven University of Technology, Eindhoven, The Netherlands, 2018.

[17] F. Yen, S. Zheng, X. Chen, J. Li, Q. Lin, Y. Xu, J. Zheng, G. Ma, J. Wang, and S. Wang, "Superconducting excitation system of a small scale linear synchronous motor," *IEEE transactions on applied superconductivity*, vol. 22, no. 3, pp. 5201103–5201103, 2011.

[18] A. Desikan, D. C. J. Krop, B. J. H. d. Bruyn, and E. A. Lomonova, "A preliminary study on superconducting linear motors in high-dynamic applications," in *11th International Conference on Power Electronics, Machines and Drives (PEMD 2022)*, vol. 2022, pp. 216–223, 2022.

[19] X. Chen, S. Zheng, J. Li, G. T. Ma, and F. Yen, "A linear induction motor with a coated conductor superconducting secondary," *Physica C: Superconductivity and its Applications*, vol. 550, pp. 82–84, 2018.

[20] L. Bertola, T. Cox, P. Wheeler, S. Garvey, and H. Morvan, "Superconducting electromagnetic launch system for civil aircraft," *IEEE Transactions on Applied Superconductivity*, vol. 26, no. 8, pp. 1–11, 2016.

[21] O. Keysan and M. A. Mueller, "A linear superconducting generator for wave energy converters," in *6th IET International Conference on Power Electronics, Machines and Drives (PEMD 2012)*, pp. 1–6, 2012.

[22] J. Li, J. Tang, and Y. Zhang, "Design of a superconducting linear synchronous motor with ybco coil magnet," *International Journal of Modern Physics B*, vol. 29, no. 25n26, p. 1542045, 2015.

[23] F. Martins, D. Dias, A. Ferreira, and R. de Andrade, "Project of a hts synchronous machine emulated by a linear motor," *IEEE Transactions on Applied Superconductivity*, vol. 25, no. 3, pp. 1–5, 2014.

[24] F. Yen, J. Li, S. Zheng, L. Liu, G. Ma, J. Wang, S. Wang, and W. Liu, "A single-sided linear synchronous motor with a high temperature superconducting coil as the excitation system," *Superconductor Science and Technology*, vol. 23, no. 10, p. 105015, 2010.

[25] J. Fang, L. Sheng, D. Li, J. Zhao, S. Li, W. Qin, Y. Fan, Q. Zheng, and W. Zhang, "Influence analysis of structural parameters and operating parameters on electromagnetic properties of hts linear induction motor," *Physics Procedia*, vol. 27, pp. 408–411, 2012.

[26] Y. Du, K. Chau, M. Cheng, Y. Wang, and J. Li, "A linear doubly-salient hts machine for wave energy conversion," *IEEE transactions on applied superconductivity*, vol. 21, no. 3, pp. 1109–1113, 2011.

[27] B. Oswald, K. Best, T. Maier, M. Soell, and H. Freyhardt, "Conceptual design of a sc hts linear motor," *Superconductor Science and Technology*, vol. 17, no. 5, p. S445, 2004.

[28] B. Oswald, K. Best, M. Setzer, E. Duffner, M. Soell, W. Gawalek, and L. Kovalev, "Ac application of hts conductors in highly dynamic electric motors," in *Journal of Physics: Conference Series*, vol. 43, p. 195, IOP Publishing, 2006.

[29] F. Lin, R. Qu, D. Li, and K. Xie, "A fully superconducting homopolar dc machine," *IEEE Transactions on Applied Superconductivity*, vol. 27, no. 4, pp. 1–5, 2017.

[30] M. Kawamura and J. A. Jones, "Superconducting super motor and generator," *IEEE Transactions on Applied Superconductivity*, vol. 27, no. 4, pp. 1–5, 2016.

[31] F. Grilli, T. Benkel, J. Hänisch, M. Lao, T. Reis, E. Berberich, S. Wolfstädter, C. Schneider, P. Miller, C. Palmer, *et al.*, "Superconducting motors for aircraft propulsion: the advanced superconducting motor experimental demonstrator project," in *Journal of Physics: Conference Series*, vol. 1590, p. 012051, IOP Publishing, 2020.

[32] J. Voccio and Q. Voccio, "Electromagnetic analysis of fully superconducting motor for electric aircraft," in *Journal of Physics: Conference Series*, vol. 1590, p. 012053, IOP Publishing, 2020.

[33] P. J. Masson and C. A. Luongo, "High power density superconducting motor for all-electric aircraft propulsion," *IEEE Transactions on Applied Superconductivity*, vol. 15, no. 2, pp. 2226–2229, 2005.

[34] T. Yanamoto, M. Izumi, M. Yokoyama, and K. Umemoto, "Electric propulsion motor development for commercial ships in japan," *Proceedings of the IEEE*, vol. 103, pp. 2333–2343, 2015.

[35] H. Koolmees, B. De Bruyn, J. Vermeulen, J. Jansen, and E. Lomonova, "The performance potential of superconducting linear and planar motors," in *17th International Conference of the European Society for Precision Engineering and Nanotechnology (EUSPEN 2017)*, pp. 465–466, European Society for Precision Engineering and Nanotechnology, 2017.

[36] H. B. Koolmees, "A superconducting magnet plate: for a planar motor application," 2020.

[37] Y. Zhang, K. Ding, and S. Du, "Design study of a high loading superconducting magnetically levitated planar motor," *IEEE Transactions on Applied Superconductivity*, vol. 31, no. 5, pp. 1–4, 2021.

[38] D. Yu, H. Liu, X. Zhang, and T. Gong, "Critical current simulation and measurement of second generation, high-temperature superconducting coil under external magnetic field," *Materials*, vol. 11, no. 3, p. 339, 2018.

[39] K. Tsuchiya, A. Kikuchi, A. Terashima, K. Norimoto, M. Uchida, M. Tawada, M. Masuzawa, N. Ohuchi, X. Wang, T. Takao, *et al.*, "Critical current measurement of commercial rebco conductors at 4.2 k," *Cryogenics*, vol. 85, pp. 1–7, 2017.

[40] F. J. Mangiarotti, M. Takayasu, and J. V. Minervini, "Ybco tape conductor characterization probe for various temperatures and fields," *IEEE transactions on applied superconductivity*, vol. 23, no. 3, pp. 9000703–9000703, 2013.

[41] Q. Wang, J. Liu, S. Song, G. Zhu, Y. Li, X. Hu, and L. Yan, "High temperature superconducting ybco insert for 25 t full superconducting magnet," *IEEE Transactions on Applied Superconductivity*, vol. 25, no. 3, pp. 1–5, 2014.

[42] L. Masur, J. Kellers, F. Li, S. Fleshler, and E. Podtburg, "Industrial high temperature superconductors: perspectives and milestones," *IEEE Transactions on Applied Superconductivity*, vol. 12, no. 1, pp. 1145–1150, 2002.

[43] W.-j. Kim, "High-precision planar magnetic levitation," *Ph. D. Thesis*, p. 6730, 1997.

[44] H.-S. Cho and H.-K. Jung, "Analysis and design of synchronous permanent-magnet planar motors," *IEEE Transactions on Energy Conversion*, vol. 17, no. 4, pp. 492–499, 2002.

[45] J. Jansen, "Magnetically levitated planar actuator with moving magnets:electromechanical analysis and design," *Reactivity of Solids*, 01 2007.

[46] I. J. Compter, "Electro-dynamic planar motor," *Precision Engineering*, vol. 28, no. 2, pp. 171–180, 2004.

[47] J. Jansen, "Preliminary investigation of a planar motor with a moving magnet configuration and with six degrees of freedom," *Master of science thesis, Eindhoven University of Technology, Eindhoven, Netherlands*, 2003.

[48] J. M. van Essen, "Design and optimization of a coreless linear actuator with three degrees of freedom," 2004.

[49] J. Jansen, C. Van Lierop, E. A. Lomonova, and A. J. Vandenput, "Magnetically levitated planar actuator with moving magnets," *IEEE Transactions on Industry Applications*, vol. 44, no. 4, pp. 1108–1115, 2008.

[50] J. de Boeij, "Multi-level contactless motion system," 2009.

[51] A. J. Hazelton, M. B. Binnard, and J.-M. Gery, "Electric motors and positioning devices having moving magnet arrays and six degrees of freedom," Mar. 27 2001. US Patent 6,208,045.

[52] D. A. Markle, "Magnetically positiond x-y stage having six degrees of freedom," Aug. 2002. US Patent 6,441,514.

[53] M. Binnard, "Planar motors with linear coils," Sept. 2002. US Patent 6,445,093.

[54] Y. Wang, F. Chen, Z. Zheng, and L. Zeng, "Magnet array of planar motor using permanent magnets with different magnetisation intensity and height," *IET Electric Power Applications*, vol. 14, no. 14, pp. 2772–2779, 2020.

[55] W. Min, M. Zhang, Y. Zhu, B. Chen, G. Duan, J. Hu, and W. Yin, "Analysis and optimization of a new 2-d magnet array for planar motor," *IEEE Transactions on Magnetics*, vol. 46, no. 5, pp. 1167–1171, 2010.

[56] J. Rovers, J. Jansen, J. Compter, and E. Lomonova, "Comparison of different topologies for a magnetically levitated planar actuator," in *Proceedings of the 8th International Symposium on Linear Drives for Industry Applications (LDIA 2011), 3-6 July 2011, Eindhoven, The Netherlands*, pp. 1–6, 2011.

[57] M. A. González and D. E. Cárdenas, "Analytical expressions for the magnetic field generated by a circular arc filament carrying a direct current," *IEEE Access*, vol. 9, pp. 7483–7495, 2020.

[58] "Presentation with measurements of the effects of force, stress and strain to the degradation of the critical current." https://www.fujikura.co.jp/eng/products/newbusiness/superconductors/01/superconductor.pdf. Accessed: 27/06/2022.

[59] "Overview of the mechanical properties of hastelloy.." https://www.haynesintl.com/alloys/alloy-portfolio_/Corrosion-resistant-Alloys/HASTELLOY-C-276-Alloy/physical-properties. Accessed: 09/12/2022.

[60] "Overview of the mechanical properties of copper.." https://www.azom.com/article.aspx?ArticleID=9017. Accessed: 09/12/2022.

[61] "Overview of kapton tape commerciably available by dupont.." https://www.dupont.com/content/dam/dupont/amer/us/en/products/ei-transformation/documents/EI-10167-Kapton-General-Specifications.pdf. Accessed: 18/07/2022.

[62] A. Korpela, T. Kalliohaka, J. Lehtonen, R. Mikkonen, J. Pitel, and P. Kovak, "Current-voltage characteristics of an hts coil having a hot spot," *IEEE Transactions on Applied Superconductivity*, vol. 12, no. 1, pp. 1438–1441, 2002.

[63] A. Ageev, I. Akirnov, A. Andriishchin, I. Bogdanov, S. Kozub, K. Myznikov, D. Rakov, A. Rekudanov, P. Shcherbakov, P. Slabodchikov, A. Seletsky, A. Shikov, V. Sytnik, A. Tikhov, L. Tkachenko, and V. Zubko,

"Test results of hts dipole," *IEEE Transactions on Applied Superconductivity*, vol. 12, no. 1, pp. 125–128, 2002.

[64] I. Hiltunen, A. Korpela, J. Lehtonen, and R. Mikkonen, "Influence of current ramp rate on voltage current measurement of a conduction-cooled hts magnet," *Physica C: Superconductivity*, vol. 468, no. 11, pp. 903–907, 2008.

[65] H. Kasahara, S. Akita, K. Tasaki, A. Tomioka, T. Hase, K. Ohata, N. Ohtani, and H. Sakaguchi, "Basic characteristic evaluation of cryocooler-cooled hts coils," *IEEE Transactions on Applied Superconductivity*, vol. 12, no. 1, pp. 766–769, 2002.

[66] S. Hahn, D. K. Park, J. Bascunan, and Y. Iwasa, "Hts pancake coils without turn-to-turn insulation," *IEEE Transactions on Applied Superconductivity*, vol. 21, no. 3, pp. 1592–1595, 2011.

[67] A. Susin, M. da Silveira, *et al.*, "An analytical method to predict the static performance of a planar actuator," *IEEE Transactions on magnetics*, vol. 39, no. 5, pp. 3364–3366, 2003.

[68] J. W. Jansen, "Magnetically levitated planar actuator with moving magnets: Electromechanical analysis and design," 2007.

[69] "The discrete fourier transform in 2d," in *Texts in Computer Science*, pp. 343–366, Springer London, 2008.

[70] F. Weidling, D. Datla, V. Petty, P. Krishnan, and G. Minden, "A framework for rf spectrum measurements and analysis," in *First IEEE International Symposium on New Frontiers in Dynamic Spectrum Access Networks, 2005. DySPAN 2005.*, p. 47, IEEE, 2005.

[71] J. W. Jansen, "Magnetically levitated planar actuator with moving magnets: Electromechanical analysis and design," pp. 32–36, 2007.

[72] L. Yan, L. Zhang, T. Wang, Y. Shang, and Z. Jiao, "Back-iron effect of tubular linear motors with dual halbach permanent magnet arrays," in *IEEE 10th International Conference on Industrial Informatics*, pp. 574–579, IEEE, 2012.

[73] Hamers, "Actuation principles of permanent magnet synchronous planar motors:a literature survey," 2005.

[74] N. Glowa, R. Wesche, and P. Bruzzone, "Quench studies of ybco insulated and noninsulated pancake coils," *IEEE transactions on applied superconductivity*, vol. 24, no. 3, pp. 1–5, 2013.

[75] Y.-S. Jo, H.-W. Kim, J. H. Sung, S.-W. Kim, D. Kim, J. H. Kim, H. M. Kim, S.-B. Kim, and M.-S. Lim, "Electrical characteristics of smart insulation 2g hts coils based on three fabrication methods," *IEEE Transactions on Applied Superconductivity*, vol. 29, no. 5, pp. 1–5, 2019.

[76] D. S. Nickel, W. H. Fietz, K.-P. Weiss, and M. J. Wolf, "Impact of bending on the critical current of hts crossconductors," *IEEE Transactions on Applied Superconductivity*, vol. 31, no. 5, pp. 1–4, 2021.

[77] G. De Marzi, N. Allen, L. Chiesa, G. Celentano, M. Takayasu, G. Tomassetti, A. Augieri, and A. Della Corte, "Bending tests of hts cable-in-conduit conductors for high-field magnet applications," *IEEE Transactions on Applied Superconductivity*, vol. 26, no. 4, pp. 1–7, 2016.

[78] S. Otten and F. Grilli, "Simple and fast method for computing induced currents in superconductors using freely available solvers for ordinary differential equations," *IEEE transactions on applied superconductivity*, vol. 29, no. 8, pp. 1–8, 2019.

[79] Y. Kashiwazaki, A. Ishiyama, X. Wang, H. Ueda, T. Watanabe, and S. Nagaya, "Numerical evaluation of the reinforcing effect of the advanced yoroi coil structure for the hts coil," *IEEE Transactions on Applied Superconductivity*, vol. 27, no. 4, pp. 1–4, 2017.

[80] J. Xia, H. Bai, H. Yong, H. W. Weijers, T. A. Painter, and M. D. Bird, "Stress and strain analysis of a rebco high field coil based on the distribution of shielding current," *Superconductor Science and Technology*, vol. 32, p. 095005, jul 2019.

[81] H. Liu, G. Song, W. Feng, M. Qiu, J. Zhu, and S. Rao, "Strain characteristic of a toroidal hts-smes fabricated by ybco stacked-tape cables," *IEEE Transactions on Applied Superconductivity*, vol. 27, no. 4, pp. 1–5, 2017.

[82] J. JW, L. EA, D. AAH, v. d. B. PPJ, and V. AJA, "Commutation of a magnetically levitated planar actuator with moving-magnets," *IEEJ Transactions on Industry Applications*, vol. 128, no. 12, pp. 1333–1338, 2008.

[83] "Database of various commercially available superconducting tapes.." http://htsdb.wimbush.eu/. Accessed: 24/05/2022.

[84] N. Strickland, C. Hoffmann, and S. Wimbush, "A 1 ka-class cryogen-free critical current characterization system for superconducting coated conductors," *Review of Scientific Instruments*, vol. 85, no. 11, p. 113907, 2014.

[85] Y. B. Kim, C. F. Hempstead, and A. R. Strnad, "Critical persistent currents in hard superconductors," *Phys. Rev. Lett.*, vol. 9, pp. 306–309, Oct 1962.

[86] Y. B. Kim, C. F. Hempstead, and A. R. Strnad, "Magnetization and critical supercurrents," *Phys. Rev.*, vol. 129, pp. 528–535, Jan 1963.

[87] J. Watson, "Magnetization of synthetic filamentary superconductors. b. the dependence of the critical current density on temperature and magnetic field," *Journal of Applied Physics*, vol. 39, no. 7, pp. 3406–3413, 1968.

[88] F. Irie and K. Yamafuji, "Theory of flux motion in non-ideal type-ii superconductors," *Journal of the Physical Society of Japan*, vol. 23, no. 2, pp. 255–268, 1967.

[89] I. Green and P. Hlawiczka, "Pinning forces and hysteresis in type ii superconductors," in *Proceedings of The Institution of Electrical Engineers*, vol. 114, pp. 1329–1333, IET, 1967.

[90] V. Karasik, N. Vasil'Ev, and V. Ershov, "Magnetization of superconducting alloy ti-22 at.% nb," *SOVIET PHYSICS JETP*, vol. 32, no. 3, 1971.

[91] T. Johansen and H. Bratsberg, "New critical-state model for magnetization of hard type-ii superconductors," *Journal of Applied Physics*, vol. 76, no. 12, pp. 8001–8004, 1994.

[92] C. M. M. Van Lierop, "Magnetically levitated planar actuator with moving magnets: Dynamics, commutation and control design," *Eindhoven, The Netherlands*, 2008.

[93] J. Compter, "A planar motor with electro-dynamic propulsion and levitation under 6-dof control," in *Proc. 4th Int. Symp. Linear Drives for Industrial Applications*, pp. 149–152, Citeseer, 2003.

[94] R. Gupta, M. Anerella, J. Cozzolino, G. Ganetis, A. Ghosh, G. Greene, W. Sampson, Y. Shiroyanagi, P. Wanderer, and A. Zeller, "Second generation hts quadrupole for frib," *IEEE transactions on applied superconductivity*, vol. 21, no. 3, pp. 1888–1891, 2010.

[95] "Overview of kapton tape by dupont, information given by external sales company.." https://www.orionind.com/pdfs/kapton.pdf. Accessed: 18/07/2022.

[96] "Overview of available tape dimension specifications by superpower.." https://www.superpower-inc.com/specification.aspx. Accessed: 12/09/2022.

[97] S. Otten, A. Kario, A. Kling, and W. Goldacker, "Bending properties of different rebco coated conductor tapes and roebel cables at t= 77 k," *Superconductor Science and Technology*, vol. 29, no. 12, p. 125003, 2016.

[98] T. Nes, G. Kirby, G. de Rijk, M. Canale, L. Gentini, J. van Nugteren, A. Kario, and H. ten Kate, "Design of a cloverleaf-racetrack dipole demonstrator magnet with dual rebco conductor," *IEEE Transactions on Applied Superconductivity*, vol. 32, no. 6, pp. 1–5, 2022.

[99] R. Gupta, M. Anerella, J. Cozzolino, J. Escallier, G. Ganetis, M. Harrison, and P. Wanderer, "Next generation ir magnets for hadron colliders," *IEEE transactions on applied superconductivity*, vol. 13, no. 2, pp. 1351–1354, 2003.

[100] R. Weultjes, "Magneto-static feasibility study of applicability of superconducting coils for planar stages." Not-published research, March 2022.

APPENDIX

A. COMPUTE INCOMPLETE ELLIPTICAL INTEGRALS

Elliptical integrals are often solved by a power series expansion. This method yields an accurate result, although the computation time is relatively long. The main goal with the semi-analytical model is to obtain a first-order approximation of the magnetic

field of a superconducting coil matrix with a low computation time. Therefore the computation time of the incomplete elliptical integrals is significantly decreased by obtaining the value from a look-up table by interpolation. Where the computation of 100.000 elements by a power series takes 1207 seconds, whereas the approximation by interpolation from a look-up-table takes 0.02 seconds. The range for the incomplete elliptical integral parameter m spans from 0 to 1, and θ spans from $-\frac{3\pi}{2}$ up to π. Where a grid of 100 by 100 points is sufficient to keep the relative discrepancy below 0.02%. Except for the grid for the parameter m should be increased to 300 points for the incomplete elliptical integral of the first kind $\mathbf{F}(\phi', m)$.

B. Measurement Data of HTS Tape

A publicly available dataset of the University of Wellington [83] is used to model the critical current limit of the superconducting tape. Where the setup and testing procedures used to measure the critical current limit of the superconducting tape is described in [84]. The aforementioned dataset comprises of measurements sampled at various operating conditions, such as: angle of the magnetic field, operating temperature of the superconducting tape and strength of the magnetic field. This dataset comprises of one of the largest set of samples for commercially available tapes, although the measurement samples just extend up to a maximum magnetic field strength of 7 T. Throughout the years several models have been proposed to describe the critical current as a function of the magnetic field [85]–[90]. A similar method was implemented in [91] to model the critical current of a YBCO superconductor. Where the critical current I_c is equal to

$$I_c = c_1 + \frac{c_2}{1 + |\frac{B}{c_3}|}, \tag{32}$$

where c_1, c_2, and c_3 are fit parameters to the measurement samples. This method has been used to fit the equation by non-linear least squares curve fitting on the available measurement data from the Wellington database in a range from 1 up to 7 T. An expected extension has been applied ranging from 7 up to 25 T for an operating temperature of 30 K, which is shown in Fig. 10.

To verify the obtained results evaluation data for higher field strengths is obtained by the manufacturer and by the research institution Fermilab. Although the results from Fermilab where measured at a slightly higher operating temperature of 33 K instead of 30K. When the extended data is compared to the expected results measured by the manufacturer and Fermilab it should be noted that the results start to diverge for larger magnetic field strengths. Thereby making this method not applicable for the extension of a high magnetic field strength. A modified version of this

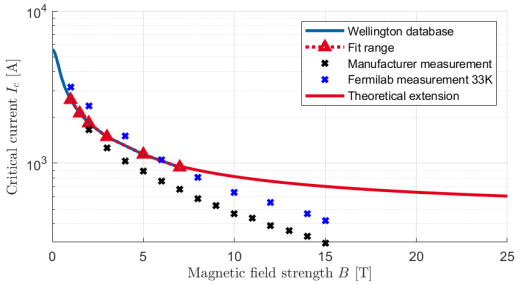

Figure 10: Result of extension of the database at a temperature of 30K with the model given by (32).

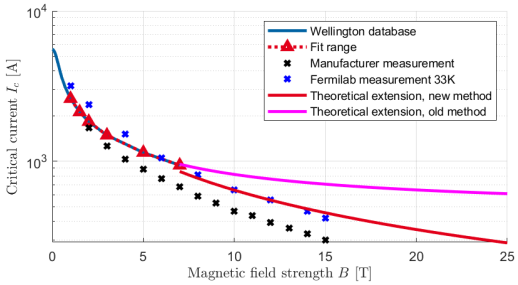

Figure 11: Result of extension of the database at a temperature of 30K with the model given by (33).

method is introduced where the critical current I_c is given by

$$I_c(B) = \frac{c_1}{1 + |\frac{B}{c_2}|}, \tag{33}$$

where c_1, and c_2 are fit parameters to the measurement samples. This method is implemented and the new theoretical extension shows a better correlation to the expected evaluation data shown by Fig. 11

C. Derivation of HTS Coil Pitch

The HTS coil dimensions are derived from the mover coil topology and the pole ratio associated with the mover coil topology. First, the associated size of the squircle coil mover topology will be assessed, followed by the racetrack coil mover topology. A mover width w_{mover} of 330mm [56] will be considered to allow for comparison to recent generation planar actuator designs.

Squircle Coil Mover Topology

The squircle coil mover topology consists of a grid of 4x4 squircle coils, shown by Fig. 12. For the given topology a pole ratio of $\frac{3}{2}\ \frac{\tau_m}{\tau_{hts}}$ is used [68], which is shown by Fig. 12. In total 6 stator poles should be present in the mover, for a mover width of 330mm the HTS coil pitch should be equal to 55mm.

Racetrack Coil Mover Topology

The racetrack coil mover design proposed by [93] is used, where the mover consists of 4 forcers. Each

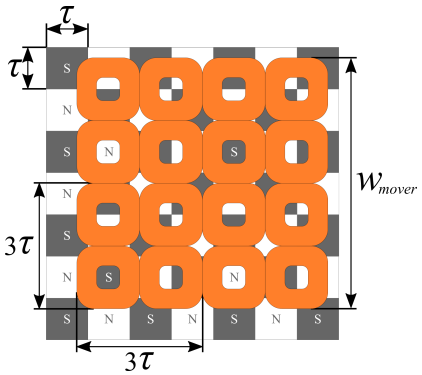

Figure 12: Overview of a squircle coil mover topology based on the work presented in [92].

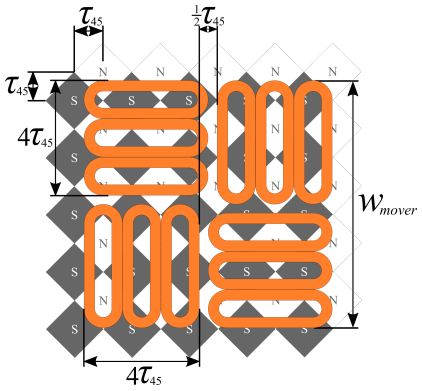

Figure 13: Overview of the used racetrack mover coil geometry.

forcer consists of a set of 3 racetrack coils and produces a vertical force and a force perpendicular to the length of the mover coils as shown by Fig. 13. Each adjacent forcer is oriented perpendicular to the adjacent forcer, this ensures force production in the other direction. Additionally, a forcer gap between two forcers is required of $\frac{1}{2}$ stator pole pitch τ_{45}. To compensate for unwanted disturbance torque which is only compensated when both forcers produce the same amount of force, this condition can be fulfilled during the acceleration of the mover [93]. The mover to stator pole ratio $\frac{\tau_m}{\tau_{45}}$ used with this mover topology is equal to $\frac{4}{3}$ [68], where τ_m is the pitch of the mover coils and τ_{45} is the pole pitch of the 45 degrees rotated HTS coils. Hence in total 8.5 stator pole pitches should be included resulting in an overall HTS coil pitch τ_p of 54.9mm.

D. Analysis on the required gap between HTS-coils

The required gap between the coils is predominantly determined by the tolerances of the HTS tape, where the thickness tolerance of $\pm 15\mu$m for 100μm tape [94]. The tolerance of the co-winding material should be added, where DuPont states a tolerance of ± 1.5 μm for 7.5μm thick Kapton tape [95]. The minimum HTS tape thickness is equal to 50μm [96] taking the additional thickness tolerance from [94] into consideration. Combined with the minimum Kapton thickness an overall minimum co-winding thickness of 57.5μm can be achieved.

The minimum internal diameter of the HTS coil is equal to 10mm, which is limited by the minimum bending radius for a substrate thickness of 50μm [58], [97]. Therefore the maximum number of turns $n_{turns,max}$ for an HTS coil pitch 55mm should equal 390 turns for a co-winding thickness of 57.5μm.

The thickness tolerance for the HTS tape σ_{hts} is equal to $\pm 15\mu$m [94], and the thickness tolerance of the Kapton tape σ_k is equal to $\pm 1.5\mu$m. The required coil gap due to total tape tolerances g_{tol} is equal to

$$g_{tol} = 2\sqrt{n_{turns,max}\left(\sigma_{hts}^2 + \sigma_k^2\right)}. \tag{34}$$

A minimum gap on each side the coil of 0.6 mm is required for a total of 390 turns. Hence making the minimum coil-to-coil gap equal to 1.2mm.

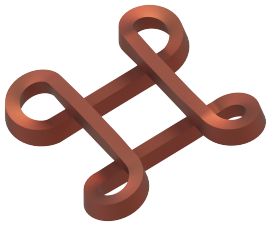

Figure 14: Overview of a squircle coil design

E. Non implemented single coil designs

Various coil designs have been researched, where not all coil designs have been taken into consideration in the research. The following single coil designs were taken into consideration, although due to the complexity or manufacturability these have not been researched or modelled.

Cloverleaf coil

The cloverleaf coil is proposed in [98], this geometry allows for straight sections around the centre of the coil. To accommodate these straight sections the overpass/underpass coil end design idea is used from [99]. The centre section and the coil end design of the cloverleaf design creates a relatively homogeneous field directly above the centre section, however the regions between the coil end designs contain a magnetic field with varying direction in a single section. This does not allow the cloverleaf design to be used to implement multiple coil sections simultaneously. Thus only the centre section could be used to produce the magnetic field, in combination with the end windings which utilize relatively much space due to the overpass/underpass design with the minimum bend radius of the coil making this design less efficient for high force density applications.

Figure-8 coil

The figure-8 coil design consists of two square coils as shown in Fig. 15, which are intertwined. Twisting of the coil section by 180 degrees is applied to allow for winding with constant tension. And the underpass/overpass design of the coil leads to two levels for the two intertwined coils. As a consequence, the space efficiency of stacked geometries of figure-8 coils is reduced by the dual-level design of the coil. Thereby making the figure-8 coil design only suitable for relatively large coils, since a minimum length is required

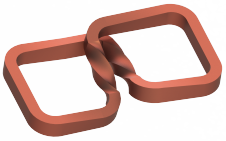

(a) Top view on figure-8 coil.

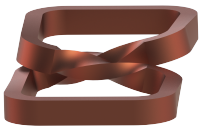

(b) Side view on figure-8 coil.

Figure 15: Overview of a figure-8 coil design.

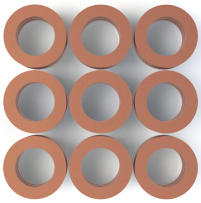

(a) Pancake coils

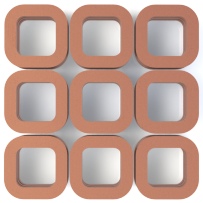

(b) Squircle coils.

Figure 16: Overview of different coil designs in a coil array configuration.

to accommodate for the twisting of the coil section by 180 degrees. Additionally, the twisting of the coil section might also lead to a less optimal magnetic field angle for the superconducting tape, thereby reducing the force density capability of the coil.

F. Non implemented coil array designs

Various coil array configurations have been taken into consideration, although the following coil configurations have not been researched due to complexity or manufacturability.

Coil arrays consisting of stacked geometries

The various coil designs can be integrated into an array to produce a matrix of alternating pole polarity. These coil designs can have various forms, such as shown in Fig. 16. It should be noted that the squircle and especially the inner-wound coil geometry allow for more effective use of the available surface area. Additionally, these coil geometries could be stacked to increase the produced magnetic field strength. This could be applied for stacks of single coil designs such as for pancake coils or squircle coils as shown in Fig. 17.

Coil arrays consisting of Halbach-inspired coil arrays

The application of vertically oriented coils might prove useful in the application of stacked geometries. Since the relative angle of the magnetic field with respect to the tape's angle might be more advantageous in comparison to horizontally oriented coil geometries. An example of vertically oriented coils combined with a stacked coil geometry is shown in Fig. 18. These vertically oriented coils could also be manufactured from other coil shapes such as two inner-wound squircle coils as depicted in Fig. 19.

(a) Pancake coils.

(b) Squircle coils.

Figure 17: Overview of stacked geometries of various coil designs.

Figure 18: Vertically oriented coil design in combination with a stacked coil geometry.

Figure 19: Stacked geometry in combination with convoluted vertically oriented coils.

G. Obtaining the Magnetic Field Optimum for a Permanent Magnet Plate

A parameter sweep is performed, to find a magnet size combination that yields a high magnetic field performance ψ_{pm} given by (29). In this parameter sweep, the magnet size ratio $\frac{\tau_m}{\tau}$, and the magnet height are swept up to a magnet height of 100mm for a pole pitch of 55mm. Where the results of this sweep are shown in Fig. 20, which shows that a magnet height above 100mm yields a diminishing increase in terms of ψ. A best magnet size ratio of 0.696 is found when the magnet size is limited up to a height of 100mm, this yields a value for ψ of 8.67 mT m. This optimum value for a permanent magnet design of ψ_{pm} will form the benchmark of the performance that could be expected of a permanent magnet plate.

Table III: Overview of the used current sheet dimensions and mesh discretisation quality.

Description	Value
Bending radius inner turn	5 mm
Inner coil width	29.5 mm
Current sheet spacing	1 mm
Number of current sheets	11
Current sheet height	12 mm
Simulation current	1000 A
Number of average quality elements	0.64 %
Number of good quality elements	22.31 %
Number of excellent quality elements	77.05 %

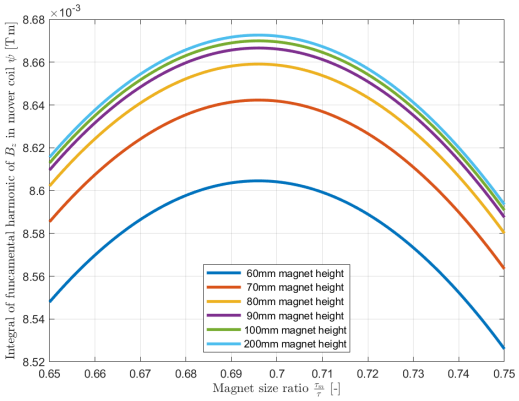

Figure 20: Overview of the integral in the mover coil height of the fundamental harmonic of B_z for a parameter sweep of the permanent magnet dimensions.

H. Verification of the Modelled Magnetic Field

This appendix shows the modelling accuracy of the Biot-Savart-based model and compares the result to a FEM simulation performed by Altair Flux. The magnetic field simulations are compared for a squircle coil, where the magnetic field is analysed 10mm above the coil. The coil in consideration is shown by Fig. 21, which consists of 11 current sheets with an inner coil width of 29.5mm and a current sheet spacing of 1mm. The coil height is equal to 12mm, the minimum bending radius is 5mm, the turns are equally spaced, and the simulation current is 1000A. All of the coil dimensions are shown in Tab. III, as well as the discretisation quality of the mesh. It should be noted that the current sheets are modelled in Altair Flux as non-meshed elements with a thickness of 1μm. The magnetic field is simulated by the Biot-Savart-based model and the FEM simulation where the results for B_x, B_y, and B_z are respectively shown in Fig. 22, 23, and 24. In these figures, the current sheets are drawn by yellow lines. To give an indication of where discrepancies are present between both modelling strategies. Fig. 22c shows the discrepancy between both modelling strategies of approximately 0.3mT for the B-field in the x-direction. The B-field in the y-direction shows a similar discrepancy, which is shown by Fig. 23c. The discrepancy in the z-direction for both models is shown in Fig. 24c, a discrepancy of 50μT is simulated for the magnetic flux density in the z-direction.

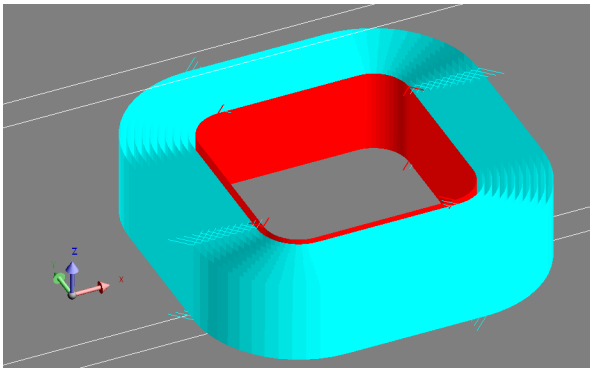

Figure 21: Overview of the modelled coil by Altair Flux

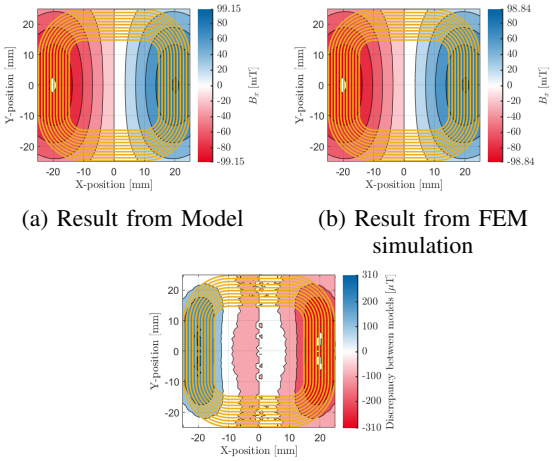

(a) Result from Model

(b) Result from FEM simulation

(c) Discrepancy between model and FEM simulation

Figure 22: Comparison of the magnetic field simulation in the x-direction between the model and a FEM simulation, simulated 10mm above a squircle coil depicted by the yellow lines.

I. Evaluation of the Current Redistribution Effect To The Magnetic Field In the Air Gap

The effect of a non-homogeneous current distribution to the B_z field in the air gap is evaluated, based on the work presented in [100]. This non-homogeneous current distribution is caused by the electrical resistivity which is dependent on the self-created magnetic field, this is also referred to as current redistribution.

To evaluate the effect on the modelling accuracy of the magnetic field in the air gap a comparison is created where a model with current distribution is evaluated to a model similar to the method presented in this paper. A single insulated circular HTS coil is simulated, according to the dimensions shown by Tab. IV. The simulation with current redistribution is simulated in COMSOL, which is provided by ir. A. Desikan. The current density distribution inside the HTS-material is shown in Fig. 25, which shows that most of the current density is located near the center of the tape width. The model with a homogeneous current density distribution proved a modelling accuracy of 0.1% of B_z in the air gap located at 10mm above the top of the coil, compared to a FEM simulation performed in

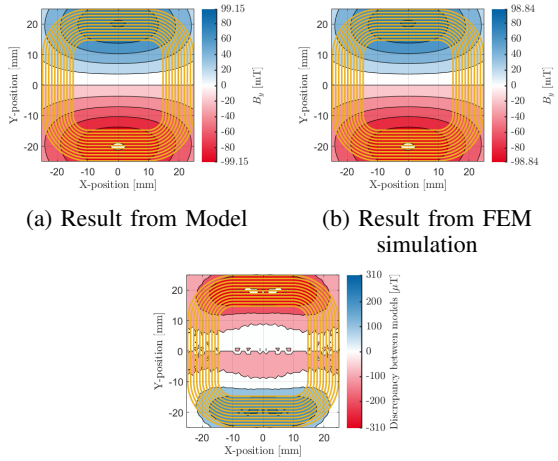

(a) Result from Model

(b) Result from FEM simulation

(c) Discrepancy between model and FEM simulation

Figure 23: Comparison of the magnetic field simulation in the y-direction between the model and a FEM simulation, simulated 10mm above a squircle coil depicted by the yellow lines.

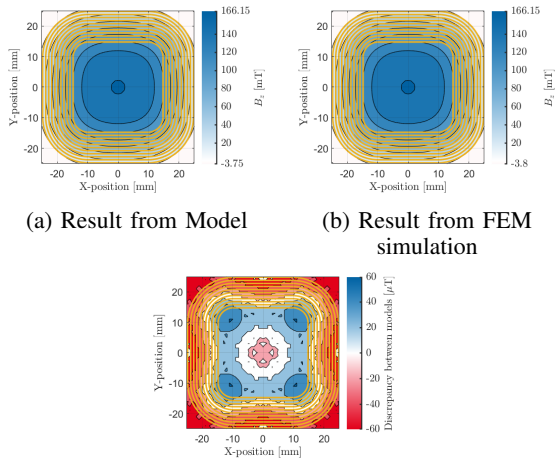

(a) Result from Model

(b) Result from FEM simulation

(c) Discrepancy between model and FEM simulation

Figure 24: Comparison of the magnetic field simulation in the z-direction between the model and a FEM simulation, simulated 10mm above a squircle coil depicted by the yellow lines.

Table IV: Overview of the used coil specifications in the model evaluation of the introduced discrepancy, due to the homogeneous current density distribution.

Dimension	Value	Unit
Inner radius	12.5	mm
Outer radius	25	mm
Tape width	4	mm
Turns	120	-
Insulation type	insulated tape	-
Tape manufacturer	Superpower	-
Tape Variant	SCS-AP	-
Simulation current	[32, 64]	A

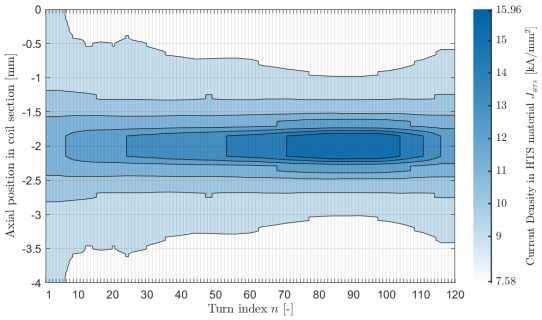

Figure 25: FEM simulation performed in COMSOL of the current density distribution inside the HTS material at a temperature of 77K, and a current of 64A.

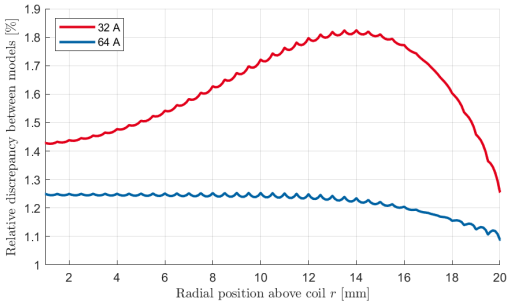

Figure 26: Discrepancy of the B_z field between the homogeneous model and current distribution model, observed 10mm above the coil section in a radial line at 32A and 64A.

Altair Flux. The discrepancy of the B_z field in the air gap is evaluated between the model with homogeneous current density distribution and homogeneous current density distribution which is shown in Fig. 26. The discrepancy is shown for a simulation current of 32A and for 64A, which is close to the quench current of the coil at an operating temperature of 77K. For the simulation current of 32A the maximum relative discrepancy between both models is equal to 1.8%, and for a simulation current of 64A the maximum relative discrepancy is equal to 1.3%. This indicates that the modelling discrepancy reduces when the coil is operated closer to the quench limit.

Although these results do not scale equal when the operating conditions or the coil geometry is changed, due to the highly non-linear properties of the HTS material. Additionally, other factors such as the deformation of the coil due to the Lorentz forces or the interaction of the magnetic field created by the mover could lead to different results. Hence these results only give an indication of the modelling discrepancy introduced by considering a homogeneous current density distribution.